

# Self-Amplification of Oxidative Stress with Tumor Microenvironment-Activatable Iron-Doped NanoplatforM for Targeting Hepatocellular Carcinoma Synergistic Cascade Therapy and Diagnosis

**Qiao-Mei Zhou**

Zhejiang University School of Medicine Second Affiliated Hospital

**Yuan-Fei Lu**

Zhejiang University School of Medicine Second Affiliated Hospital

**Jia-Ping Zhou**

Zhejiang University School of Medicine Second Affiliated Hospital

**Xiao-Yan Yang**

Zhejiang University School of Medicine Second Affiliated Hospital

**Xiao-Jie Wang**

Zhejiang University School of Medicine Second Affiliated Hospital

**Jie-Ni Yu**

Zhejiang University School of Medicine Second Affiliated Hospital

**Yong-Zhong Du**

Zhejiang University College of Pharmaceutical Sciences

**Ri-Sheng Yu** (✉ [risheng-yu@zju.edu.cn](mailto:risheng-yu@zju.edu.cn))

Zhejiang University School of Medicine Second Affiliated Hospital <https://orcid.org/0000-0003-0554-9484>

---

## Research

**Keywords:** organic/inorganic nanoplatforM, Ferroptosis, Chemodynamic therapy, Magnetic resonance imaging, hepatocellular carcinoma.

**Posted Date:** July 9th, 2021

**DOI:** <https://doi.org/10.21203/rs.3.rs-684204/v1>

**License:** © ⓘ This work is licensed under a Creative Commons Attribution 4.0 International License.

[Read Full License](#)

# Abstract

## Background

The rapid development of hepatocellular carcinoma (HCC) treatment resistance has become a technical bottleneck for clinical treatment. Conventional chemotherapy has long been regarded as ineffective against HCC because of the insensitivity to chemotherapy drugs. Ferroptosis is a form of programmed cell death with a definite Fenton reaction mechanism that converts endogenous hydrogen peroxide ( $H_2O_2$ ) into highly toxic hydroxyl radicals ( $\cdot OH$ ). Therefore, we have developed an ultrasensitive iron-doped magnetic mesoporous silica nanoplatfrom (DOX@Fe-HMON-Tf NPs) for HCC-targeted synergistic cascade therapy and diagnosis.

## Results

This organic/inorganic nanoplatfrom consists of a silica shell doped with iron and bis[3-(triethoxysilyl)propyl]tetrasulfide (BTES) and the etched core loaded DOX that generate  $H_2O_2$  in situ to enhance the ferroptosis effect. DOX@Fe-HMON-Tf NPs can effectively internalized into hepatoma cells by precise delivery through the transferrin grafted with polyethylene glycol (PEG) outside the shell. The resulting nanoplatfrom can be activated by the tumor microenvironment (TME) in which the glutathione (GSH)-responsive biodegradability could synergize with the therapeutic interaction between DOX and iron and induce tumor cells death through complementary ferroptosis and apoptosis mechanisms. At the same time, the nanoplatfrom has a superparamagnetic framework that can be used for treatment guidance and monitoring under the guidance of  $T_2$ -weighted magnetic resonance imaging (MRI).

## Conclusion

The rationally designed nanoplatfrom provides a new strategy for anti-tumor effects with self-amplified synergistic chemotherapy and chemodynamic therapy (CDT) based on ferroptosis, and magnetic resonance imaging that realizes the integration of diagnosis, treatment and monitoring.

## Background

Hepatocellular carcinoma (HCC) has been ranked as the fourth leading cause of cancer-related mortality worldwide (ranked second among men) [1]. Although early detection and monitoring programs are recommended, only 30%-40% of patients are diagnosed at an early stage and are eligible for curative-intent treatments such as surgical resection, ablation or liver transplantation [2]. Most cases of HCC still progress to the intermediate or advanced stage of disease with no treatment, and the median survival time is less than two years [3]. Doxorubicin (DOX) is still the most commonly chemotherapy drug for the treatment of intermediate or advanced HCC [4]. However, conventional chemotherapy has long been regarded as ineffective against HCC because of the insensitivity to chemotherapy drugs [5, 6]. More

emerging treatment methods are needed to supplement existing treatment options to improve the treatment effect of HCC.

Ferroptosis is a kind of programmed cell death pattern discovered in recent years, which relies on iron and reactive oxygen species (ROS) to induce lipid peroxidation [7]. Ferroptosis depends on highly harmful hydroxyl radicals ( $\cdot\text{OH}$ ), the most chemically reactive species of ROS, generated by catalyzing endogenous hydrogen peroxide ( $\text{H}_2\text{O}_2$ ) through  $\text{Fe}^{2+} / \text{Fe}^{3+}$  produced by the Fenton reaction to kill tumor cells [8, 9]. The unstable iron pool in the tumor cells catalyzes the production of ROS through the Fenton reaction, resulting in effective chemodynamic therapy (CDT). Compared with photodynamic therapy and sonodynamic therapy, there is no external energy and oxygen involved, extremely broadening the application range of free radical-mediated tumor therapy [10, 11]. Viswanathan's group reported that cancer cells with therapy-resistant state are more sensitive to ferroptosis [12], which meaning they are more likely to be killed by ferroptosis compared with non-therapy-resistant cancer cells [13]. Unfortunately, the efficiency of this strategy is limited by relatively low concentration of iron, insufficient endogenous  $\text{H}_2\text{O}_2$  and increased tumor antioxidant defense capabilities [14, 15].

Although tumor cells have high  $\text{H}_2\text{O}_2$  levels, it's still not enough to produce ample  $\cdot\text{OH}$  to achieve satisfactory CDT efficacy [16, 17]. In order to increase the  $\text{H}_2\text{O}_2$  level in the tumor microenvironment (TME), one strategy is delivering  $\text{H}_2\text{O}_2$  to the tumor area directly by nanocarriers [18], and the other strategy is to quickly and efficiently generate  $\text{H}_2\text{O}_2$  by delivering glucose and oxygen to the tumor tissue [19, 20]. However, the former cannot continuously supply  $\text{H}_2\text{O}_2$ , while the latter is limited by the intrinsic hypoxia inside tumor tissue. These factors cut down the therapeutic effect of CDT in solid tumors. In addition, high concentration of glutathione (GSH) is one of the characteristics of TME. As an important antioxidant in cells, GSH can eliminate the generated ROS in some way and weaken the efficiency of CDT [21, 22]. These inevitable obstacles imply that the simultaneous introduction of  $\text{H}_2\text{O}_2$  supply and GSH elimination functions into a nanoplatfrom is expected to produce effective CDT.

Interestingly, the chemotherapy drug DOX not only can induce tumor cells death by inhibiting DNA replication but also produce  $\text{H}_2\text{O}_2$  by activating nicotinamide adenine dinucleotide phosphate oxidase (NOXs) [23]. DOX treatment can further increase  $\text{H}_2\text{O}_2$  levels, which is the substrate of Fenton reaction, promoting the ferroptosis process. Therefore, the combination of DOX and  $\text{Fe}^{2+}/\text{Fe}^{3+}$  is expected to efficiently induce CDT. Currently,  $\text{Fe}^{2+}/\text{Fe}^{3+}$  redox pair-based Fenton reaction-mediated biocatalytic tumor therapy has been widely used for tumor-specific iron delivery [24, 25]. Furthermore,  $\text{Fe}^{2+}$  can trigger ferroptosis through varieties ways except the Fenton reaction, including iron-catalyzed oxidation of polyunsaturated fatty acids or auto-oxidation of lipids [26, 27]. Because the ferroptosis induced by  $\text{Fe}^{2+}$  can circulate in the cell membrane through the Haber-Weiss reaction chain, the newly emerging lipid radicals can further attack the adjacent unsaturated fatty acids to trigger another lipid radical chain reaction [28]. This automatic amplification process catalyzed by  $\text{Fe}^{2+}$  can spread membrane destruction and ferroptosis damage when the molecular protection that controls lipid peroxidation fails. However, due

to the relatively high oxidation sensitivity of  $\text{Fe}^{2+}$ , coupled with the regulation of the ferroptosis process, there are fewer reports on the application in ferroptosis-based tumor treatment. Therefore, the development of ferroptosis-based nanoplatform with tumor targeting and controllable pharmacokinetic properties have an important clinical significance for enhancing anti-tumor efficacy and reducing health risks [29].

Mesoporous silica nanoparticles (MSN NPs) have attracted extensive research attention as drug carriers for their potential biomedical applications [30, 31]. Inorganic nanomaterials have high chemical/physiological stability and versatility, but their biocompatibility and biodegradability are lower than organic nanomaterials [32, 33]. The construction of organic/inorganic hybrid material nanoplatform is expected to combine the advantages of both and overcome their respective shortcomings, thus showing broad prospects for clinical applications [34]. To satisfy the above multifaceted requirements, biocompatible and biodegradable hollow mesoporous organosilica nanoparticles (HMON NPs) have been successfully constructed via selective introduction of bis[3-(triethoxysilyl)propyl]tetrasulfide (BTES) [35]. The thioether-hybridized HMON NPs are chosen for efficient delivery of DOX owing to their GSH-responsive biodegradability and controlled release of anti-tumor drugs.

According to the specific coordination properties between introduced  $\text{Fe}^{2+}/\text{Fe}^{3+}$  with Fe-coordination proteins, doping biocompatible  $\text{Fe}^{2+}/\text{Fe}^{3+}$  into silica framework (Fe-HMON NPs) could further improve its biodegradability [36]. However, traditional iron delivery nanomaterials usually exhibit nonspecific effects, which are mainly delivered through enhanced permeability and retention effects may cause significant side effects when applied in vivo [37]. Transferrin is an endogenous protein that can transport  $\text{Fe}^{3+}$  to cells with overexpression of transferrin receptor [38]. Due to abnormal iron metabolism, transferrin receptor is overexpressed in HCC cells [39]. Grafting naturally occurring transferrin onto the surface of Fe-HMON NPs through polyethylene glycol (PEG) serves as a target ligand (Fe-HMON-Tf NPs), which can reduce the phagocytosis of the reticuloendothelial system, retain the high permeability and retention effect of solid tumors, enhancing the specific targeting of the nanoplatform [40]. Furthermore, Fe-based nanoparticles traditionally serve as  $T_2$ -weighted magnetic resonance imaging (MRI) contrast agents [41]. Fe-HMON-Tf NPs show superparamagnetic and  $T_2$ -MRI performance that enable further therapeutic guidance and monitoring.

Herein, we propose an intelligent iron-doped hollow mesoporous organosilica nanoplatform that possesses  $\text{H}_2\text{O}_2$  self-supplying, GSH eliminating properties for efficient CDT based on ferroptosis to inhibit tumor growth by TME-activatable sequential catalytic reactions. The iron-doped mesoporous silica nanoparticles with huge cavities can effectively load the DOX that not only serve as chemotherapy, but also increase the production of  $\text{H}_2\text{O}_2$  in tumor cells. The surface-modified transferrin is specific to the transferrin receptor highly expressed on the HCC to achieve targeted tumor delivery and high accumulation of DOX. The intelligent iron-doped hollow mesoporous organosilica nanoplatform can disintegrate under the action of abundant GSH in TME and trigger the rapid release of DOX, thereby significantly improving the inhibitory effects, reducing toxicity side effects and improving the tolerance.

At the same time, the consumption of GSH, the Fenton reaction of  $\text{Fe}^{2+}/\text{Fe}^{3+}$  and the supply of  $\text{H}_2\text{O}_2$  by DOX in situ can trigger the ferroptosis of HCC cells, realizing coordinated cascade of chemotherapy and CDT. The multifunctional nanoplatform is expected to reverse the drug resistance of translational therapy, inhibit the recurrence and metastasis of HCC, and realize the clinical integration of accurate diagnosis, accurate treatment and real-time monitoring.

## Experimental Section

### Materials

Cetyltrimethylammonium chloride (CTAC), triethanolamine (TEA), bis[3-(triethoxysilyl) propyl]tetrasulfide (BTES), tetraethyl orthosilicate (TEOS), (3-mercaptopropyl)trimethoxysilane (MPTES), ferrous acetylacetonate and transferrin were purchased from Sigma-Aldrich (MO, USA). Doxorubicin (DOX), deferiprone, urea, 3-(4,5Dimethylthiazol-yl)-2,5Dimethylthiazol-2-yl)-2,5diphenyltetrazolium bromide (MTT), *N*-(3-dimethylaminopropyl)-*N*-ethylcarbodi imide hydrochloride (EDC), *n*-hydroxysuccinimide (NHS), L-Glutathione (GSH), silane-PEG-COOH (Mw = 2000) were purchased from Aladdin Reagent Database Inc (Shanghai, China). 4',6-Diamidino-2-phenylindole (DAPI), indocyanine green (ICG) was obtained from Tokyo Chemical Industry (Tokyo, Japan). Fetal bovine serum (FBS) and Dulbecco's Modified Eagle's Medium (DMEM) were obtained from Gibco (USA). All other chemicals and solvents were of analytical or chromatographic grade. Deionized water (18.4 M $\Omega$ cm) used in all experiments was prepared using a Milli-Q system (Millipore, Boston, USA) and was used in all experiments.

### Synthesis of mesoporous organosilica nanoparticles (HMON NPs)

To start with, CTAC aqueous solution (20g, 10 wt. %) and TEA aqueous solution (3.5g, 10 wt.%) were first mixed and stirred at 80°C, and then TEOS (1ml) was added dropwise for 1h reaction. Subsequently, a mixture of TEOS (0.5ml) and BTES (1ml) was added for another 4h of reaction. The resultant products were collected after centrifugation and washed with ethanol several times. Afterward, the products were dispersed in methanol (30 mL) with NaCl (1 wt.%) to extract the template and the extraction procedure was repeated at least three times to guarantee the template was removed completely. For synthesis of HMON NPs, an ammonia-assisted selective etching strategy was used. The above products were dispersed in 30mL of water with a certain amount of ammonia solution and react for 3h at 95°C. The final HMON NPs were obtained by centrifugation and washed with ethanol several times.

### Synthesis of Fe-doped hollow mesoporous organosilica nanoparticles (Fe-HMON NPs)

Then, HMON NPs (25mg) and ferrous acetylacetonate (200mg) were dissolved completely in urea ethanol solution (25ml) and homogenized for 5 min under ultrasound treatment. The mixture was transferred to a water bath and reacted for 12 h at 80°C. The resultant Fe-HMON NPs were collected by centrifugation and washed with an ethanol-deionized water solution (v: v 1:1) several times.

# Synthesis of Fe-HMON-PEG NPs and Fe-HMON-PEG-Tf NPs

For the PEGylation of Fe-HMON NPs, Fe-HMON NPs (20mg) were dissolved into ethanol (30ml), followed by the addition of silane-PEG-COOH (30mg) with magnetic stirring under 78°C for 12 h. After the reaction, Fe-HMON-PEG NPs were obtained after centrifugation and washed with ethanol for several times. Then activating the -COOH groups to conjugate with transferrin. EDC (12mg) and NHS (15mg) were added to Fe-HMON-PEG NPs (20mg) suspended in 20ml PBS. The mixture was carried out in an Erlenmeyer flask under stirring at 37°C for 4h. The products were centrifuged with PBS three times to remove excess EDC and NHS polymer. Then added transferrin solution (200ul, 1mg/ml) to the products and reacted for 12h at 37°C with shaking. Fe-HMON-PEG-Tf NPs were collected by centrifugation and washed with PBS three times.

## Characterization

The particle size and size distribution were measured by Dynamic light scattering (DLS, litesizer500, Anton-Paar, Austria). The morphology of the MSN NPs, HMON MSN NPs and Fe-HMON MSN NPs were observed by transmission electron microscopy (TME, JEM-1200EX, JEOL, Japan). X-ray diffraction (XRD) patterns were recorded by a D/MAX-2550 PC diffractometer using Cu K $\alpha$  radiation with a 2 $\theta$  range of 10°-80° (Rigaku Inc., Japan). Fourier transmission infrared (FTIR) spectra of nanoparticles were performed using a FTIR spectroscopy (VECTOR22, Bruker, Germany) in the range from 400 to 4000cm<sup>-1</sup>. The distributions and proportions of Fe, O, Si were performed using energy-dispersive spectroscopy (EDS) elemental mapping (X-MAX<sup>n</sup>65 T, Oxford, UK). Nitrogen adsorption/desorption experiment was tested by using a Micromeritics Tristar II analyzer (Micromeritics, USA). The surface areas and average pore size distributions were calculated by Brunauer-Emmett-Teller (BET) and Barrett-Jyner-Halenda (BJH) methods. The valence state of iron analysis was performed on the x-ray photoelectron spectrometer (XPS, ESCALAB 250Xi, Thermo Fisher Scientific, UK).

## Drug loading and release profiles

The encapsulation of DOX by HMON-Tf NPs, Fe-HMON-PEG NPs and Fe-HMON-Tf NPs were prepared by simply mixing the DOX (3mg) with nanoparticles s (10mg) in PBS solution for 24h under the dark conditions. After that the unloaded DOX was removed by centrifugation and the supernatants were reserved for the calculation of loading efficiency of drugs.

$$\square \text{ Loading content} = (\text{TD} - \text{FD}) / \text{TN} \times 100\%$$

$$\square \text{ Encapsulation efficiency} = (\text{TD} - \text{FD}) / \text{TD} \times 100\%$$

where TD is the total weight of DOX fed, FD is the weight of nonencapsulated free DOX, and TN is the weight of nanoparticles.

To study the dissociation of DOX@ Fe-HMON-Tf NPs in response to pH and GSH trigger. DOX@Fe-HMON-Tf NPs were dispersed into buffer solutions of different pH values (pH 7.4 and pH 5.5) and different GSH

concentration (5mM and 10mM) at a concentration of 0.5 mg/ml. After predetermined periods of time, 0.2ml of the incubation solution was extracted and centrifuged at 12000 rpm for 15 min to remove undissolved nanoparticles. The concentration of DOX in the supernatant was detected by a fluorescence spectrophotometer. And the content of iron in the supernatant was determined by inductively coupled plasma mass spectrometry (ICP-MS) instrument (ICAPRQICPMS, Thermo Fisher, USA).

## **In vitro and in vivo MRI**

The Fe concentration of Fe-HMON-Tf NPs were determined by ICP-MS. With deionized water as a control group, samples with various Fe concentrations (0, 0.036, 0.072, 0.288, 0.576, 1.152mM) were dispersed in deionized water. All these were placed in 2mL Eppendorf tubes and measured with a 3T MRI scanner (Discovery MR 750, GE, USA) to obtain  $T_2$ -weighted MRI. Through fitting plots of the inverse relaxation times  $1/T_2 \text{ s}^{-1}$  vs Fe concentration (mM), the relaxation coefficients  $r_2$  was obtained.

$T_2$ -weighted MRI was performed on a 3 T MRI scanner with a small-animal coil. Anesthetized mice bearing tumors were scanned using a fast spin-echo sequence pre- and post-injection of nanoparticles via the tail vein, with the following scan parameters: repetition time 3000ms, time to echo 80ms, field of view 40×40mm, matrix size 250×250, and slice thickness 2mm.

## **MTT assay on the cytotoxicity of various nanosamples**

HepG2 cell line and LO2 cell line were obtained from the Chinese Academy of Sciences cell bank (Shanghai, China). Cells were cultured in Dulbecco's Modified Eagle Medium (Gibco, USA) supplemented with 10% FBS (Gibco, USA) and 1% penicillin-streptomycin (Gibco, USA) in a 37°C incubator with 5% CO<sub>2</sub>. Cells were subcultured regularly using trypsin/EDTA (Meilune, China). The mediums were refreshed every 2 days. The HepG2 cells were seeded onto a 96-well plate at density of  $10^4$  U per well and subsequently incubated overnight at 37°C under an atmospheric CO<sub>2</sub> level of 5%. The incubation media were then replaced with fresh ones containing PBS, DOX, HMON-Tf NPs, Fe-HMON-Tf, NPs DOX@HMON-Tf NPs, DOX@Fe-HMON-PEG NPs and DOX@Fe-HMON-Tf NPs. The equivalent concentrations of DOX were maintained at 0.25,0.5,1,1.5,2,2.5,3,3.5µg/ml. Each nanosample group contained six wells, and the incubation periods were set to 24 h. Fresh media containing MTT agents (0.5mg/ml) were added into each well when the incubation was complete and incubated for 4h. Afterwards, unreacted dyes were carefully removed by aspiration, and 150µL DMSO was added to each well to dissolve the formazan crystals. After 10min of low-speed oscillation, the OD value was measured using a Microplate reader (Bio-Rad, Model 680, USA) at a wavelength of 570nm.

## **Evaluation on the cellular uptake of the nanosamples**

For the cellular uptake evaluations, the HepG2 cells were seeded into a six-well plate at a density of  $10^5$  U per well and incubated in 2ml of medium overnight at 37°C under an atmospheric CO<sub>2</sub> level of 5%. When the cell confluence reached around 70%, fresh media containing PBS, DOX, HMON-Tf NPs, Fe-HMON-Tf NPs, DOX@HMON-Tf NPs, DOX@Fe-HMON-PEG NPs and DOX@Fe-HMON-Tf NPs were used to replace the exhausted medium. The nanosamples concentration were maintained at 20µg/ml and the

equivalent concentrations of DOX were maintained at 2 $\mu$ g/ml, the incubation periods were set to 24h. When the incubation completed, the cells were washed three times with PBS, fixed with 4% paraformaldehyde solution, stained with DAPI and finally analyzed by confocal laser scanning microscopy (CLSM; SP8 TCS, Leica, Germany) observation.

## **Quantification of the intracellular iron level**

HepG2 cells were first seeded onto six-well plates at a density of  $10^5$  U per well, and the incubation conditions were kept the same with the in vitro experiments above. When the cell confluence reached around 70%, the previously added mediums were replaced by new ones containing PBS, DOX, HMON-Tf NPs, Fe-HMON-Tf NPs, DOX@HMON-Tf NPs, DOX@Fe-HMON-PEG NPs, DOX@Fe-HMON-Tf NPs. The concentration of nanosamples was 20 $\mu$ g/ml, and the equivalent DOX concentration was maintained at 2 $\mu$ g/ml. The incubation would continue for 24h. Subsequently, the culture medium in all wells was removed, and the cells were washed three times with PBS. The cells were then detached by trypsin without EDTA-Na and purified twice by repetitive centrifugation and PBS washing. Cell lysate (containing 1% SDS, 1% Triton X-100, and 40mM tris acetate) was eventually added to lyse the cells, and the resultant solution was sonicated to ensure complete cell disintegration. The iron level was detected by ICP-MS as above.

## **Monitoring the level of H<sub>2</sub>O<sub>2</sub> in tumor cells**

The HepG2 cells were seeded into a six-well plate using exactly the same protocol as above. The medium in each well were replaced with fresh ones containing different concentrations of DOX (0, 0.125, 0.25, 0.5, 1, 2 and 5 $\mu$ g/ml) when the cell confluence reached around 70%. The incubation would last for 24 hours, then intracellular H<sub>2</sub>O<sub>2</sub> level was examined using the standard Fluorimetric Hydrogen Peroxide Assay Kit (Sigma-Aldrich), for which the fluorescent probe was first added to each well and the cells were further incubated for 20min at 37°C. The red fluorescent product has an excitation wavelength of 540nm and an emission wavelength of 590nm, which were used for the observation of the intracellular H<sub>2</sub>O<sub>2</sub> levels analyzed by CLSM observation.

## **Evaluation of the intracellular lipoperoxide**

HepG2 cells were seeded into six-well plates as described above and treated with various samples when the cell confluence reached 70%. PBS, DOX, HMON-Tf NPs, Fe-HMON-Tf NPs, DOX@HMON-Tf NPs, DOX@Fe-HMON-PEG NPs, DOX@Fe-HMON-Tf NPs. The incubation lasted for 24 hours, the concentration of nanosamples was 20 $\mu$ g/ml and the equivalent DOX concentration was maintained at 2 $\mu$ g/ml. When the incubation was complete, the cells were washed twice with PBS and incubated with DOPIBY C11 (Lipoperoxide indicator; concentration, 5 $\mu$ M) for 30min. The intracellular level of lipoperoxides was monitored using a CytoFLEX flow cytometry system (Beckman Coulter). A same experimental setup was also used for the CLSM observations.

## **Monitoring the changes in mitochondrial membrane potential**

HepG2 cells were seeded into six-well plates as described above and treated with PBS, DOX, HMON-Tf NPs, Fe-HMON-Tf NPs, DOX@HMON-Tf NPs, DOX@Fe-HMON-PEG NPs, DOX@Fe-HMON-Tf NPs when the cell confluence reached 70%. The incubation lasted for 24h, and the concentration of nanosamples was 20µg/ml, and the DOX concentration was at 2µg/ml. When the incubation was complete, the tumor mitochondria were stained with JC-1 dye following the procedures provided in the user manual and then observed by CLSM.

## **Flow cytometric analysis of the cell apoptosis**

HepG2 cells were seeded into a six-well plate at the density of  $10^5$ U per well. When the cell confluence reached 70%, the mediums were replaced with fresh ones containing PBS, DOX, HMON-Tf NPs, Fe-HMON-Tf NPs, DOX@HMON-Tf NPs, DOX@Fe-HMON-PEG NPs, DOX@Fe-HMON-Tf NPs and the incubation would continue for 24h. The concentration for all nanoparticles were 20µg/ml, and the DOX concentration in each group was maintained at an equivalent level of 2µg/ml. The media were drained when the incubation was complete, and the cells were washed three times with PBS and subsequently detached using non-EDTA-Na-containing trypsin. The detached cells were purified twice by repetitive washing and centrifugation. The cell apoptosis was investigated by flow cytometry using the Annexin V-FITC/PI apoptosis detection kit (Sigma) via the protocol.

## **Intracellular GSH assay**

HepG2 cells were seeded in six-well plates at the density of  $10^5$ U per well and incubated until the cell confluence reached 70%. Then the mediums were replaced with fresh ones containing PBS, DOX, HMON-Tf NPs, Fe-HMON-Tf NPs, DOX@HMON-Tf NPs, DOX@Fe-HMON-PEG NPs, DOX@Fe-HMON-Tf NPs and the incubation would continue for 24h. Afterwards, the cells were harvested and washed with PBS thrice. Then cell lysates were collected and measured according to the instructions of GSH and GSSG Assay Kit. A UV-vis spectrophotometer (TU-1800PC, Beijing Purkinje General Instrument Co., Ltd., China) was used to measure the absorbance at 412nm to determine the GSH levels.

## **Intracellular GPX-4 activity assay**

Intracellular GPX-4 activity was measured using a cellular glutathione peroxidase assay kit (Beyotime, Jiangsu, China). HepG2 cells were seeded in a six-well plate and cultured at 5% CO<sub>2</sub>, 37°C overnight. Then the mediums were replaced with fresh ones containing PBS, DOX, HMON-Tf NPs, Fe-HMON-Tf NPs, DOX@HMON-Tf NPs, DOX@Fe-HMON-PEG NPs, DOX@Fe-HMON-Tf NPs and the incubation would continue for 24h. The cell lysates were collected and measured according to the manufacturer's instructions. The M5 full-band multi-function microplate reader (SynergyMx M5, Molecular Devices, USA) was used to measure the absorbance at 340nm.

## **Western blot assays**

To determine the expression levels of the apoptotic protein of Caspase-3 and the ferroptosis-related proteins of GPX4. HepG2 cells were seeded into six-well plates at a density of  $10^5$ U per well and incubated overnight at 37°C under an atmospheric CO<sub>2</sub> level of 5% until the cell confluence reached

around 70%. Subsequently, the mediums were replaced by fresh ones containing PBS, DOX, HMON-Tf NPs, Fe-HMON-Tf NPs, DOX@HMON-Tf NPs, DOX@Fe-HMON-PEG NPs, DOX@Fe-HMON-Tf NPs and further incubated for 24h. The concentration of nanosamples was 20 $\mu$ g/ml, and the DOX concentration was 2 $\mu$ g/ml. The cells were then lysed with Laemmli Sample Buffer (Bio-Rad), and the total protein was quantified by electrophoresis using a BCA protein kit (Beyotime) and 12% SDS–polyacrylamide gel electrophoresis. The proteins were then transferred from the gel onto polyvinylidene difluoride membrane (Immobilon P, Millipore) and blocked by primary and secondary antibodies. The images were captured on a molecular imager (ChemiDoc Touch Imaging System, Bio-Rad, USA).

## Tumor model

Balb/c nude mice were (4–5 weeks, ~ 15g) were purchased from Shanghai Silaike Laboratory Animal Co., Ltd. All animal experiments were carried out in accordance with the National Institutes of Health (NIH, USA) guidelines for the care and use of laboratory animals in research. The surgical procedures and experiment protocols were approved by the Committee for Animal Experiments of Zhejiang University. The HepG2 tumor models were established by injecting 100 $\mu$ l of PBS containing 10<sup>7</sup>U of HepG2 cells into the subcutaneous tissue of the mice. The tumor volume was calculated as  $V_{\text{tumor}} = LW^2/2$  (L, maximum diameter of the tumor; W, minimum diameter of the tumor, both were measured using a digital vernier caliper).

## Fluorescence imaging for tracking nanosamples in vivo

The evaluation of biodistribution was performed by using subcutaneous tumor bearing BALB/C nude mice (6 mice/group). The near infrared dye ICG was used to label the Fe-HMON-PEG NPs and Fe-HMON-Tf NPs before intravenous injection. The equivalent ICG concentration was maintained at 1mg/kg. The mice were anaesthetized at different time points, and then their fluorescent photographs were captured by the IVIS Spectrum Imaging System (Caliper, PerkinElmer, USA). In addition, the mice were euthanized by CO<sub>2</sub> asphyxiation at 24h post-injection, and then their major organs (tumor, heart, liver, spleen, lung and kidney) were collected, which were then imaged to observe the fluorescence signals.

## Tumor treatment effect and histology analysis

The therapeutic efficacy of different treatment was evaluated using subcutaneous HepG2 tumor-bearing mice. Various samples were then administrated when the tumor size reached 60mm<sup>3</sup>, and the initial weight of all mice was maintained at 18.2  $\pm$  0.2g. Briefly, 42 HepG2 tumor-bearing mice were randomly divided into seven groups (each with six mice). The sample groups are PBS, DOX, HMON-Tf NPs, Fe-HMON-Tf NPs, DOX@HMON-Tf NPs, DOX@Fe-HMON-PEG NPs, DOX@Fe-HMON-Tf NPs. All samples were injected through the tail vein at an equivalent DOX concentration of 5mg/kg. The injection was repeated every other day, and the body weight and tumor volume of nude mice were both recorded. After 21 days of treatment, all mice were euthanized, and the tumors and major organs were harvested for the subsequent analysis. Typically, the organs and tissues were sectioned and embedded into paraffin after being fixed with 10% formalin at 4 $^{\circ}$ C for 24h, and then, paraffin-embedded sections were stained with H&E to monitor the cytotoxicity induced by various nanoplateforms. In addition, the tumor sections were

also stained by the colorimetric TUNEL Apoptosis Assay Kit to determine the therapeutic effect. Both the H&E- and TUNEL-stained tissue sections were then observed with a microscope.

For the survival analysis, 42 HepG2 tumor-bearing mice were treated using the above procedures. No more injection was given after 21 days, and the number of live mice in each group was recorded until day 60.

## Statistical analysis

SPSS ver. 26.0 (IBM Inc., USA) and GraphPad Prism ver. 9.0 (GraphPad Software, USA) were used to process all data. Quantitative experimental data are recorded as means  $\pm$  SD. We used the two-tailed t test or the Mann-Whitney U test to compare two groups and the Kruskal-Wallis test to perform multiple comparisons. Statistical significance was set at  $P < 0.05$ .

## Result And Discussion

### Construction and characterization of the TME-activatable iron-doped nanoplatfrom

The synthesis scheme and biomedical application of the tumor-targeting TME-activatable iron-doped hollow mesoporous organosilica nanoplatfrom was illustrated (Fig. 1 a and b). In brief, the core/shell structure of thioether hybrid mesoporous silica nanoparticles (HMON NPs) was constructed based on the chemical homology principle through the co-hydrolysis and co-condensation of bis[3-(triethoxysilyl)propyl]tetrasulfide (BTES) and tetraethoxysilane by cetyltrimethylammonium chloride (CTAC) as the structural-directing and pore-forming agent, triethanolamine (TEA) as the alkaline catalyst and tetraethyl orthosilicate (TEOS) as the silica precursor [35, 42]. The disulfide-bridged HMON NPs obtained by using mild ammonia instead of strong HF/NaOH as the etching agent because of the Si-C bonds within the shell are more stable and stronger than the Si-O bonds within the core [43]. Then during the hydrothermal treatment process, the ferrous acetylacetonate ( $\text{Fe}(\text{acac})_2$ ) can react with the released silicon-containing oligomers (dissolution process) to form a Fe-doped silica layer on the surface of HMON NPs (growth process), which called the "dissolution-growth" strategy to prepare Fe-HMON NPs.

Transferrin (Tf) was grafted onto the surface of Fe-HMON NPs by silane-PEG-COOH to enhance the targeting (Fe-HMON-Tf NPs). DOX was effectively loaded into Fe-HMON-Tf NPs through charge adsorption and complexation with  $\text{Fe}^{2+}/\text{Fe}^{3+}$ , and the loading capacity up to 20.21% as well as the complexation can minimize the sensitivity to oxidative stress before  $\text{Fe}^{2+}$  release in the cell. The transmission electron microscopy (TEM) images showed that unetched HMON NPs, HMON NPs and Fe-HMON NPs had a spherical shape with an average size of around 40nm (Fig. 2a, b and c).

The result showed that the size of the nanoparticles didn't change significantly after Fe-doped. According to the dynamic light scattering results, the average hydrodynamic diameter of Fe-HMON-PEG NPs were around 56nm and Fe-HMON-Tf NPs were around 71nm (Fig. S1a). The presence of mesopores within the

shell of HMON NPs and Fe-HMSN NPs were demonstrated by the N<sub>2</sub> adsorption–desorption isotherms. The Brunauer-Emmett-Teller (BET) surface area of HMSN NPs were 352.2 m<sup>2</sup> g<sup>-1</sup> and the pore size around 4.1 nm as well as the surface area of Fe-HMSN NPs were 292.2 m<sup>2</sup> g<sup>-1</sup> and the pore size around 3.3 nm (Fig. S2a and b). Fe-HMSN NPs exhibited a large surface area and mesopore size that allowed for sufficient encapsulation of various kinds of payloads. In addition, Fourier transform infrared spectroscopy (FTIR) was also used to investigate and confirm the change of chemical composition after each modification step (Fig. S3b). Specifically, the specific strong and broad peaks at 1120 cm<sup>-1</sup> attributed to Si-O bond and the peak at 485 cm<sup>-1</sup> in the spectra confirmed the successful construction of the disulfide-bridged Fe-HMON NPs nanostructure. After the coating of PEG, a new peak has appeared at 1660 cm<sup>-1</sup>, which was due to the stretching vibration of the C = O bond of carboxyl. Amide I and II bands at 1562 cm<sup>-1</sup> and 1720 cm<sup>-1</sup> of Tf coated nanoparticles suggested the successful introduction of protein molecules. The modification-induced changes in the surface properties of the nanoplateforms were also consistently confirmed by the UV–vis spectroscopy (Fig. S3a) and zeta potential analysis (Fig. S1b).

In addition, the Fe-HMON NPs have also been characterized with energy-dispersive spectroscopy (EDS) to study the elemental composition. The results showed the distribution of silicon, oxygen, iron, and sulfur in the nanostructure (Fig. 2d) and implicated the successful introduction of iron into the silica framework. And the engineered iron amount was determined to be 27.30% by inductively coupled plasma (ICP) measurement. In order to predict the stabilization efficiency of Fe<sup>2+</sup> of Fe-HMON NPs on potential oxidative stress *in vivo*, the valence distribution of iron was quantitatively analyzed by comparing the fitting peak area of X-ray photoelectron spectroscopy (XPS). The fitting results of the Fe 2p<sub>3/2</sub> spectra showed two characteristic peaks that the peak at 709.5 eV was attributed to Fe<sup>2+</sup> while the peak at 712.9 eV was caused by Fe<sup>3+</sup> (Fig. 2e). It can further prove that Fe<sup>2+</sup> was dominant in Fe-HMON NPs by comparing the fitting peak areas that Fe<sup>2+</sup> was much higher than Fe<sup>3+</sup>. The Fe<sup>2+</sup> in the Fe-HMON NPs framework had high oxidation resistance because of the chemical bonding, which is highly beneficial for inducing ferroptosis *in vivo*.

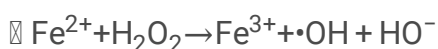
## Profiling release behaviors of the TME-activatable iron-doped nanoplateform

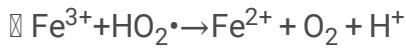
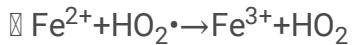
The thioether hybrid HMON NPs were selected for biomedical applications due to their reductive responsive biodegradability due to in-frame disulfide bond cleavage triggered by GSH [44]. Interestingly, the coordination of iron and protein would make the silica framework rich in reaction sites and further accelerated the biodegradation of the silica framework [45]. As shown by high-resolution transmission electron microscopy and selected area electron diffraction characterizations (Fig. 2f and g), the Fe-HMON NPs were in an amorphous state and potentiating rapid degradation when exposed to the TME. Besides, x-ray diffraction (XRD) pattern of Fe-HMON NPs showed a single broad peak at 2 $\theta$  = 23° (Fig. 2h), representing a typical amorphous phase. The use of the prepared composite nanoplateform to achieve ferroptosis-based tumor therapy basically depended on the effective release of DOX and Fe<sup>2+</sup>/Fe<sup>3+</sup> from DOX@Fe-HMON-Tf NPs.

Therefore, we first studied the release characteristics of DOX and Fe<sup>2+</sup>/Fe<sup>3+</sup> by incubating DOX@Fe-HMON-Tf NPs in the buffer solution. Specifically, under the physiological pH of 7.4, DOX@Fe-HMON-Tf NPs showed excellent chemical stability where the total DOX leakage after 24 hours of incubation was low as 20%. The release percentage around 30% when incubating at pH 5.5 for 24 hours, which suggesting the sensitivity of the nanoplatform to acidic pH slightly (Fig. 3a). Moreover, the release percentage around 65% when incubating in 5mM GSH solution at pH 5.5 for 24 hours, while the release percentage was 82% in 10mM GSH solution at pH 5.5. Since the disulfide bonds in the Fe-HMON-Tf NPs framework tend to be cleaved in the reducing TME, it was found that Fe-HMON-Tf NPs were gradually degraded in a mimic GSH solution[46]. The release profile of iron was also measured via inductively coupled plasma mass spectrometry (ICP), and the trends were similar except that the release rates were slower. The results showed that iron release percentage was less than 20% after incubating at pH 7.4 and pH 5.5 for 7 days, while under 5mM GSH solution and 10mM GSH solution at pH 5.5, the release percentage increased to above 57.5% and 74.4% (Fig. 3b). Additional, DOX@Fe-HMON-Tf NPs after incubation have also been collected for TEM observation, and it was found that the severity of structural degradation for nanoplatform was positively correlated to the amount of accumulative iron release. The nanoplatform has splintered into small pieces when the incubation period was extended to 7 days in 5mM GSH solution and 10mM GSH solution at pH 5.5 while the small pieces gradually disappear when extended to 14 days (Fig. 3c). These images again validated the degradability of the whole composite nanoplatform in physiological conditions. Furthermore, the biodegradation behavior of DOX@Fe-HMSN-Tf NPs were assessed in fetal bovine serum (FBS), which similar to the components of human serum, containing numbers of proteins coordinatively to Fe<sup>2+</sup>/Fe<sup>3+</sup> [47]. It was found that DOX@Fe-HMON-Tf NPs underwent rapid biodegradation in FBS that large amounts of degradation products could be found after 5d of biodegradation (Fig. S4). This phenomenon was due to the coordination effects to the Fe<sup>2+</sup>/Fe<sup>3+</sup> by the proteins in FBS, which extracted the iron from DOX@Fe-HMSN-Tf NPs and further accelerated the biodegradation of silica framework. Summary, DOX@Fe-HMON-Tf NPs exhibited time-dependent biodegradable behaviors.

## Evaluation on the cytotoxicity profiles of nanosamples in vitro

Fe-HMON-Tf NPs were co-incubated with HepG2 liver tumor cell line 24 hours under varied conditions to validate the biocompatibility and therapeutic efficacy. It has been found that HMON-Tf NPs showed no substantial cytotoxicity towards HepG2 cells while Fe-HMON-Tf NPs displayed concentration-dependent cytotoxicity. For instance, the viability of HepG2 cells dramatically decreases to as low as 37.6% in the presence of 50 µg/mL of Fe-HMON-Tf NPs. Comparatively, the HMON-Tf NPs were non-cytotoxic even in high concentration (Fig. S5a). The reason may be the Fenton reaction triggered by Fe<sup>2+</sup>/Fe<sup>3+</sup>, which produced highly toxic free radicals harmful to HepG2 cells.





What's more, the abundant  $\text{Fe}^{3+}$  from the nanoplatfrom can be transformed to  $\text{Fe}^{2+}$  by the high-level of intracellular GSH, which greatly enhance the production of ROS and the CDT effects [48].

## **MRI capabilities analysis of nanosamples**

The superparamagnetic framework endowed the DOX@Fe-HMON-Tf NPs with potential contrast property for  $T_2$ -weighted MRI, which was favorable for the guidance and monitoring of tumor treatment. The nanoplatfrom presented the  $r_2$  relaxivity of  $22.2 \text{ mM}^{-1} \text{ s}^{-1}$  (Fig. 4a and b). Furthermore, in vivo contrast-enhanced MRI of HepG2 tumor-bearing nude mice were performed at pre, 0h, 2 h and 6h post intravenous administrations of DOX@Fe-HMON-Tf NPs. The signal in tumor tissue decreased substantially after the DOX@Fe-HMON-Tf NPs injection, which could be attributed to the targeting ability and their  $T_2$ -weighted MRI performance (Fig. 4c). The wonderful  $T_2$ -weighted MRI performance of Fe-HMON-Tf nanoplatfrom promised the following therapeutic guidance and monitoring.

## **Evaluation on the uptake efficiency of nanosamples by HepG2 cells**

Confocal laser scanning microscopic (CLSM) images directly showed that DOX@Fe-HMON-Tf NPs could efficiently deliver DOX into HepG2 cells, as demonstrated by the intracellular red fluorescence of DOX molecules. Although DOX@Fe-HMON-PEG NPs without transferrin modification was partially taken up by HepG2 cells, treated with DOX@Fe-HMON-Tf NPs showed higher DOX accumulation (Fig. 5a). This was expected because we have previously demonstrated that the transferrin receptor was overexpressed in HepG2 cells [49]. In addition, the nanoplatfrom-induced intracellular iron accumulation was also investigated directly with ICP. It could be observed that the trends in the intracellular iron levels were highly consistent with that of the DOX fluorescence, where the iron concentration in the DOX@Fe-HMON-Tf NPs group has increased by 40% approximately compared to DOX@Fe-HMON-PEG NPs (Fig. 5b).

## **Investigation on the generation of lipoperoxide induced by nanosamples**

In general, ferroptosis is the direct result of lipid peroxide accumulation, and its execution is essentially dependent on cellular iron overload. Simultaneously increasing the levels of iron and  $\text{H}_2\text{O}_2$  in tumor cells can be a promising strategy to effectively initiate and execute ferroptosis. Various reports have consistently shown that DOX could not only directly damage DNA in tumor cells but also generate high level of  $\text{H}_2\text{O}_2$  by activating the intracellular NADPH oxidase 4 (NOX4) [50]. Since the activity of NOX4 is mainly regulated by its abundance, it is expected that up-regulation of NOX4 induced by DOX could enhance the production of  $\text{H}_2\text{O}_2$  in the intracellular environment and thus support the initiation and propagation of lipid peroxidation. Here, we first investigated the effectiveness of DOX-induced  $\text{H}_2\text{O}_2$

generation by incubating HepG2 cells with varying concentrations of DOX and subsequently monitoring the intracellular levels of  $H_2O_2$ . The results collectively demonstrated that the intracellular levels of  $H_2O_2$  in HepG2 cells increased obviously when the amount of administered DOX between  $1\mu\text{g/ml}$  to  $2\mu\text{g/ml}$  (Fig, 5c), while no obvious change was observed in the intracellular concentration of lipidperoxide at the same time (Fig, S6a and b). In comparison, when the HepG2 cells were incubated with the iron-containing sample series, the lipid peroxidation level has increased in a similar manner to the intracellular  $H_2O_2$  concentration. The flow cytometric analysis was the direct evidence of ferroptosis induced by DOX@Fe-HMON-Tf NPs and supported the enhanced absorption capacity of Tf-modified nanoplatfrom by tumor cells (Fig. 5d). Moreover, the DOX@Fe-HMOIN-Tf NPs showed the highest level in HepG2 cells (Fig. 5e), which evidently supported the occurrence of lipid peroxidation.

## Investigation on the change of mitochondrial membrane potential induced by nanosamples

Mitochondria is the main place that most human cells produce energy and many programmed cell death pathways converge. Recent studies have shown that ferroptosis is also accompanied by mitochondrial hyperpolarization due to the accumulation of ROS[28]. Consequently, we measured the changes in the mitochondrial membrane potential of HepG2 cells using the JC-1 assay kit, which showed red color when the membrane potential was positive but turned to green when the membrane potential decreased. Therefore, the color changes of the mitochondria JC-1 staining could indicate the severity of cellular damage caused by different treatments. According to the CLSM results (Fig. 5f), the HepG2 cells treatment with free DOX caused yellow-green fluorescence after 24 hours of incubation. In contrast, cells treated by DOX@Fe-HMON-Tf NPs demonstrated strong green fluorescence, which was obviously due to the introduction of ferroptosis-inducing iron species and suggested the highly negative mitochondrial membrane potential. The results showed that mitochondria are highly sensitive to lipid peroxidation shortly after the onset of ferroptosis stimulus.

## Evaluation on the efficacy of the dual ferroptosis/apoptosis tumor therapy in vivo

The cytotoxic activity of the composite nanoplatfrom on HepG2 cells was investigated using 3-(4,5)-dimethylthiaziazolo(-z-y1)-3,5-di-phenyltetrazoliumro-mide (MTT) assay, in which the DOX concentrations were maintained the same. The results revealed that the free DOX showed greater cytotoxicity to HepG2 cells than the other nanosamples when the incubation period was 24 hours. Specifically, the survival rate of HepG2 cells incubated with DOX@Fe-HMON-Tf NPs group was low as 43.1% at the DOX concentration of  $2\mu\text{g/ml}$ , while the cells survival rate of the free DOX group was still high as 55.3% under the same concentration at 24 hours (Fig. S5b).

Using flow cytometry to further study the details revealed by the MTT assay (Fig. 6a). The flow cytometric analysis revealed that the total ratio of dead cells in HepG2 cells after incubation with DOX@Fe-HMON-Tf NPs group for 24 hours was high as 38.1%, while in the free DOX group was only 28.6% in HepG2 cells.

These results clearly proved the superior therapeutic efficacy by combining ferroptosis therapy and DOX comparing to conventional chemotherapeutic strategies.

## Investigation on the therapeutic mechanism of the nanoplatform

Then, we tried to determine the cell death mechanism involved in the treatment of DOX@Fe-HMON-Tf NPs through a variety of complementary technologies. From a mechanistic point, the treatment with DOX would up-regulate the expression level of NOX4 and increase the generation of  $H_2O_2$  [51], which could provide the iron mediated peroxidation and further contribute to ferroptosis. The rupture of the disulfide bond in the nanostructure and the high-state  $Fe^{3+}$  can oxidize GSH to oxidized glutathione (GSSG). Among the PBS, HMON-Tf NPs, Fe-HMON-Tf NPs groups, the GSH content in the Fe-HMON-Tf NPs group was lowest, followed by HMON-Tf NPs group and PBS group was the highest, indicating that the nanoplatforms entering the cells can effectively consume GSH (Fig. 6b). To ensure membrane integrity and minimize the damage caused by ROS, lipid hydroperoxide glutathione peroxidase 4 (GPX4) uses reduced GSH as a cofactor to convert lipid hydroperoxide (R-OOH) into lipid alcohol (R-OH). This process prevents the formation and accumulation of iron-dependent toxic lipid ROS [52, 53]. Depleting the intracellular GSH pool to reduce GPX4 activity and elevating lipid peroxidation level lead to ferroptosis ultimately. Thus, we investigated the changes in the expression and activity of GPX4 in HepG2 cells after nanoplatforms treatment. Because the synthesis of GSH was inhibited after HepG2 cells were co-incubated with disulfide-bridged nanoplatforms. As co-incubated with Fe-HMON-Tf NPs disulfide-bridged HMON NPs, the activity of GPX4 decreased obviously (Fig. 6c), and the protein expression level decreased substantially (Fig. 6d). Also, DOX@Fe-HMON-Tf NPs had a higher inhibitory effect on the activity of GPX4 and the expression of GPX4 than Fe-HMON-Tf NPs. Thus, DOX may be able to down-regulate GPX4 levels together with  $Fe^{2+}/Fe^{3+}$  and disulfide bonds in some way, which leads to irresistible lipid peroxidation and ferroptosis. Meanwhile, it was observed that the expression level of caspase-3 had also increased, which was apparently due to the activation of the caspase-mediated apoptosis pathway by the concurrently delivered DOX. The above results confirmed that the death of HepG2 cells after incubation with DOX@Fe-HMON-Tf NPs were caused by the combination of ferroptosis and DOX-mediated apoptosis, and also supported the dual role of DOX as apoptosis inductor and ROS enhancer in this nanoplatform. The western blot results well supported the molecular mechanism of the synergistic ferroptosis /apoptosis induced by the DOX@Fe-HMON-Tf NPs (Fig. 6e).

## The distribution patterns of nanosamples in vivo

The distribution patterns of nanoplatforms in vivo after intravenous injection were also studied to determine their tumor specificity and delivery efficiency. For tracking these nanoparticles in vivo, the nanoplatforms were fluorescently stained with a near infrared-absorbing dye named ICG. The imaging results demonstrated that DOX@Fe-HMON-Tf NPs could be more effectively deposited into the tumor tissues compared to DOX@Fe-HMON-PEG NPs (Fig. 7a) on HepG2 tumor models. The fluorescence images of organs and tumors harvested at 24 hours in vitro and quantitative analysis of the fluorescence

patterns revealed that the total ICG fluorescence treated with DOX@Fe-HMON-Tf NPs higher than DOX@Fe-HMON-PEG NPs (Fig. 7b and c). The results could be explained by the surface modification of transferrin.

## **In vivo evaluation on the anti-tumor efficacy of ferroptosis combined with chemotherapy**

We further studied its anti-tumor efficacy separately on HepG2 tumor mouse models. Briefly, nude mice with HepG2 xenograft were divided into seven groups (six mice each) and treated with PBS, HMON-Tf NPs, Fe-HMON-Tf NPs, DOX, DOX@HMON-Tf NPs, DOX@Fe-HMON-PEG NPs, DOX@HMON-Tf NPs respectively. It was ensured that equivalent amount of DOX or nanocarriers were used in each group. By comparing the volume of tumors, it was found that the tumor suppression was the most obvious in the DOX@HMON-Tf NPs group (Fig. 8a). Specifically, the average volume of HepG2 tumors after treatment with DOX@HMON-Tf NPs for 21 days was the lowest with an average weight of 0.13 g, while the average volume and weight of the tumors in the free DOX group were 4 and 0.58 g, respectively (Fig. 8b and c). Even without the iron doping, the tumor inhibitory caused by DOX@HMON-Tf NPs were still better than free DOX in tumor models, which could be explained by the tumor-targeting capability of the nanoplatform leading to higher DOX accumulation in the tumor cells. Furthermore, the tumors were extracted and sliced for hematoxylin and eosin (H&E) and terminal deoxynucleotidyl transferase-mediated deoxyuridine triphosphate nick end labeling (Tunel) staining (Fig. 8d), the results showed that the tumor cells death were most severe in the DOX@HMON-Tf NPs group. The above data unanimously supported our hypothesis that the DOX@HMON-Tf nanoplatform could effectively inhibit tumor growth in live animal models by supplementing ferroptosis and chemotherapy.

In addition, we also comparatively investigated the potential side effects of nanoplatforms after in vivo administration. As revealed by the changes of mouse weight through the experimental period (Fig. S7a), the DOX group showed apparent weight loss after around 3 days of incubation, and the final average weight was only 19.5g, which was due to the severe toxicity caused by DOX. Contrastingly, the body weight for the DOX@Fe-HMON-PEG NPs and DOX@HMON-Tf NPs groups had remained at 20.3 and 20.6 g, which were at the same level to the PBS group (20.7g). Histological analysis of the major organs harvested from the mice in each group via H&E staining demonstrates that the free DOX had caused severe damage to the heart muscle, while no apparent histological changes were registered for mice in the DOX@Fe-HMON-PEG NPs and DOX@HMON-Tf NPs groups (Fig. S7b). The superior treatment efficacy of DOX@HMON-Tf NPs group was also supported by the survival analysis (Fig. 8e). Specifically, HepG2 tumor-bearing mice treated with DOX@HMON-Tf NPs had a median survival time of 50 days, which was much longer than the other groups. These results indicated that the DOX@HMON-Tf nanoplatform had good biocompatibility, which may greatly promote its transformation into potential clinical applications.

## **Conclusions**

In summary, we have constructed a tumor-targeting diagnostic and therapeutic nanoplatform by incorporating tetrasulfide bonds and active sites of iron into the silica framework, followed by loading of DOX to generate  $H_2O_2$  in situ for orchestrated cooperative tumor therapy. The resultant nanoplatform could be activated by GSH-rich tumor microenvironment and induce tumor cells death via complementary ferroptosis and apoptosis mechanism. Fe-HMON NPs could protect the  $Fe^{2+}$  from the oxidative stress in the biological environment and minimize the premature drug leakage before arriving at the tumor specific site to optimize the therapeutic activity. The surface modification of transferrin could endow the DOX@Fe-HMON-Tf NPs with high targeting ability to accumulate in the tumor tissues via the high affinity of transferrin with the transferrin receptor overexpressed in hepatoma cells, which could effectively T2 modal MRI-guided advance synergistic cascade hepatocarcinoma therapy and diagnosis. Mechanistic studies demonstrated that ROS produced by DOX-induced NOXs activation could act in synergy with the simultaneously released  $Fe^{2+}/Fe^{3+}$  to amplify the CDT based on ferroptosis, the dual ferroptosis and apoptosis treatment eventually lead to efficacious tumor growth inhibition. This study can overcome the limitations of conventional anti-tumor modalities and provide magnetic resonance imaging capabilities for monitoring, which expected to realize the clinical integration of accurate diagnosis, accurate treatment and real-time monitoring of hepatocellular carcinoma.

## Abbreviations

HCC: hepatocellular carcinoma, DOX: doxorubicin, PEG: polyethylene glycol, CDT: chemodynamic therapy, TME: tumor microenvironment, MRI: magnetic resonance imaging, ROS: reactive oxygen species, MSN NPs: mesoporous silica nanoparticles, HMON NPs: hollow mesoporous organosilica nanoparticles, Fe-HMON NPs: iron-doped hollow mesoporous organosilica nanoparticles, Tf: Transferrin, DOX@Fe-HMON-Tf NPs: DOX-loaded transferrin modified iron-doped hollow mesoporous organosilica nanoparticles.

## Declarations

### Acknowledgements

We would like to thank the members of Professor Du's team (Pharmacy School of Zhejiang University) for their guidance and assistance in this study.

### Authors' contributions

Qiao-Mei Zhou conceived the study and drafted the manuscript. Ri-Sheng Yu and Yong-Zhong Du helped critically revise the manuscript for important intellectual content. Qiao-Mei Zhou, Yuan-Fei Lu and Jia-Ping Zhou performed the research. Xiao-Yan Yang, Xiao-Jie Wang and Jie-Ni Yu helped analyze data. All authors read and approved the final manuscript.

### Funding

This study was supported in part by grants from the Natural Science Foundation of Zhejiang province (LY18H180003), and the National Natural Science Foundation of China (General Program: 81571662).

### Availability of data and materials

All data generated or analyzed during this study are included in this published article and its additional file.

### Ethics approval and consent to participate

All the animal experiments were in line with the ARRIVE guidelines and were carried out according to the National Institutes of Health (NIH, USA) protocols, approved by the guidelines of the Ethical Committee of Zhejiang University.

### Consent for publication

All authors agreed to submit this manuscript.

### Competing interests

The authors declare that they have no competing interests.

## References

1. Bray, F., et al., *Global cancer statistics 2018: GLOBOCAN estimates of incidence and mortality worldwide for 36 cancers in 185 countries*. *CA: a cancer journal for clinicians*, 2018. **68**(6): p. 394-424.
2. Maepa, M., et al., *Recent developments with advancing gene therapy to treat chronic infection with hepatitis B virus*. *Current opinion in HIV and AIDS*, 2020. **15**(3): p. 200-207.
3. Umeda, S., M. Kanda, and Y. Kodera, *Emerging evidence of molecular biomarkers in hepatocellular carcinoma*. *Histology and histopathology*, 2018. **33**(4): p. 343-355.
4. Lee, A.C.K., et al., *Mitochondrial Fuel Dependence on Glutamine Drives Chemo-Resistance in the Cancer Stem Cells of Hepatocellular Carcinoma*. *Int J Mol Sci*, 2021. **22**(7).
5. Yang, J.D., et al., *A global view of hepatocellular carcinoma: trends, risk, prevention and management*. *Nat Rev Gastroenterol Hepatol*, 2019. **16**(10): p. 589-604.
6. Asghar, U. and T. Meyer, *Are there opportunities for chemotherapy in the treatment of hepatocellular cancer?* *J Hepatol*, 2012. **56**(3): p. 686-95.
7. Wang, S., et al., *Arginine-Rich Manganese Silicate Nanobubbles as a Ferroptosis-Inducing Agent for Tumor-Targeted Theranostics*. *ACS nano*, 2018. **12**(12): p. 12380-12392.
8. Lu, X., et al., *Bioinspired Copper Single-Atom Catalysts for Tumor Parallel Catalytic Therapy*. *Advanced materials (Deerfield Beach, Fla.)*, 2020. **32**(36): p. e2002246.

9. Lin, L.S., et al., *Synthesis of Copper Peroxide Nanodots for H<sub>2</sub>O<sub>2</sub> Self-Supplying Chemodynamic Therapy*. J Am Chem Soc, 2019. **141**(25): p. 9937-9945.
10. Xiao, M., et al., *A photosensitizer-inhibitor conjugate for photodynamic therapy with simultaneous inhibition of treatment escape pathways*. Biomaterials, 2020. **257**: p. 120262.
11. Zhang, Y., et al., *Oxygen-carrying nanoparticle-based chemo-sonodynamic therapy for tumor suppression and autoimmunity activation*. Biomater Sci, 2021.
12. Viswanathan, V., et al., *Dependency of a therapy-resistant state of cancer cells on a lipid peroxidase pathway*. Nature, 2017. **547**(7664): p. 453-457.
13. Sang, M., et al., *Mitochondrial membrane anchored photosensitive nano-device for lipid hydroperoxides burst and inducing ferroptosis to surmount therapy-resistant cancer*. Theranostics, 2019. **9**(21): p. 6209-6223.
14. Sang, Y., et al., *Bioinspired Construction of a Nanozyme-Based HO Homeostasis Disruptor for Intensive Chemodynamic Therapy*. Journal of the American Chemical Society, 2020. **142**(11): p. 5177-5183.
15. Jana, D., et al., *Ultrasmall Alloy Nanozyme for Ultrasound- and Near-Infrared Light-Promoted Tumor Ablation*. ACS nano, 2021. **15**(4): p. 7774-7782.
16. Deng, L., et al., *Low-intensity focused ultrasound-augmented Cascade chemodynamic therapy via boosting ROS generation*. Biomaterials, 2021. **271**: p. 120710.
17. Zhou, H., et al., *Ultrasensitive Chemodynamic Therapy: Bimetallic Peroxide Triggers High pH-Activated, Synergistic Effect/H<sub>2</sub>O<sub>2</sub> Self-Supply-Mediated Cascade Fenton Chemistry*. Advanced healthcare materials, 2021. **10**(9): p. e2002126.
18. Li, W.P., et al., *Ultrasound-Induced Reactive Oxygen Species Mediated Therapy and Imaging Using a Fenton Reaction Activable Polymersome*. ACS Nano, 2016. **10**(2): p. 2017-27.
19. Hao, Y., et al., *Near-infrared light and glucose dual-responsive cascading hydroxyl radical generation for in situ gelation and effective breast cancer treatment*. Biomaterials, 2020. **228**: p. 119568.
20. Yue, L., et al., *Supramolecular nanovesicles for synergistic glucose starvation and hypoxia-activated gene therapy of cancer*. Nanoscale, 2021.
21. Fu, L., et al., *Nanocatalytic Theranostics with Glutathione Depletion and Enhanced Reactive Oxygen Species Generation for Efficient Cancer Therapy*. Advanced materials (Deerfield Beach, Fla.), 2021. **33**(7): p. e2006892.
22. Zhang, L., et al., *One-pot synthesis of a self-reinforcing cascade bioreactor for combined photodynamic/chemodynamic/starvation therapy*. Journal of colloid and interface science, 2021. **599**: p. 543-555.
23. Zhang, J., et al., *Heparanase-driven sequential released nanoparticles for ferroptosis and tumor microenvironment modulations synergism in breast cancer therapy*. Biomaterials, 2021. **266**: p. 120429.

24. Wang, Y., et al., *Ferrocene-containing polymersome nanoreactors for synergistically amplified tumor-specific chemodynamic therapy*. Journal of controlled release : official journal of the Controlled Release Society, 2021. **333**: p. 500-510.
25. Yang, Y., et al., *Blue light-triggered Fe-release from monodispersed ferrihydrite nanoparticles for cancer iron therapy*. Biomaterials, 2021. **271**: p. 120739.
26. Kagan, V., et al., *Oxidized arachidonic and adrenic PEs navigate cells to ferroptosis*. Nature chemical biology, 2017. **13**(1): p. 81-90.
27. Sun, W., et al., *Phospholipase iPLA $\beta$  averts ferroptosis by eliminating a redox lipid death signal*. Nature chemical biology, 2021. **17**(4): p. 465-476.
28. Hassannia, B., P. Vandenabeele, and T. Vanden Berghe, *Targeting Ferroptosis to Iron Out Cancer*. Cancer cell, 2019. **35**(6): p. 830-849.
29. Norouzi, M., et al., *Clinical applications of nanomedicine in cancer therapy*. Drug discovery today, 2020. **25**(1): p. 107-125.
30. Lin, F., et al., *Magnetism, Ultrasound, and Light-Stimulated Mesoporous Silica Nanocarriers for Theranostics and Beyond*. Journal of the American Chemical Society, 2021. **143**(16): p. 6025-6036.
31. Wu, Q., et al., *Surface Wettability of Nanoparticle Modulated Sonothrombolysis*. Advanced materials (Deerfield Beach, Fla.), 2021: p. e2007073.
32. Fu, Y., et al., *Poly ethylene glycol (PEG)-Related controllable and sustainable antidiabetic drug delivery systems*. European journal of medicinal chemistry, 2021. **217**: p. 113372.
33. Jin, R., et al., *Pollen-like silica nanoparticles as a nanocarrier for tumor targeted and pH-responsive drug delivery*. Talanta, 2021. **231**: p. 122402.
34. Zhao, Z., et al., *General Synthesis of Ultrafine Monodispersed Hybrid Nanoparticles from Highly Stable Monomicelles*. Advanced materials (Deerfield Beach, Fla.), 2021: p. e2100820.
35. Guo, W., et al., *Biodegradable hollow mesoporous organosilica nanotheranostics (HMON) for multi-mode imaging and mild photo-therapeutic-induced mitochondrial damage on gastric cancer*. Journal of nanobiotechnology, 2020. **18**(1): p. 99.
36. Wang, L., et al., *Iron-engineered mesoporous silica nanocatalyst with biodegradable and catalytic framework for tumor-specific therapy*. Biomaterials, 2018. **163**: p. 1-13.
37. Chen, Q., et al., *Iron-based nanoparticles for MR imaging-guided ferroptosis in combination with photodynamic therapy to enhance cancer treatment*. Nanoscale, 2021. **13**(9): p. 4855-4870.
38. Vogt, A., et al., *On Iron Metabolism and Its Regulation*. International journal of molecular sciences, 2021. **22**(9).
39. Wang, K., et al., *Protein liposomes-mediated targeted acetylcholinesterase gene delivery for effective liver cancer therapy*. Journal of nanobiotechnology, 2021. **19**(1): p. 31.
40. Cai, Y., et al., *Tumor-targeting peptide functionalized PEG-PLA micelles for efficient drug delivery*. Biomaterials science, 2020. **8**(8): p. 2274-2282.

41. Chen, J., et al., *A redox-triggered C-centered free radicals nanogenerator for self-enhanced magnetic resonance imaging and chemodynamic therapy*. *Biomaterials*, 2021. **266**: p. 120457.
42. Chen, Y. and J. Shi, *Chemistry of Mesoporous Organosilica in Nanotechnology: Molecularly Organic-Inorganic Hybridization into Frameworks*. *Adv Mater*, 2016. **28**(17): p. 3235-72.
43. Li, L., et al., *In Situ Polymerized Hollow Mesoporous Organosilica Biocatalysis Nanoreactor for Enhancing ROS-Mediated Anticancer Therapy*. *Advanced functional materials*, 2020. **30**(4).
44. Guo, W., et al., *Biodegradable hollow mesoporous organosilica nanotheranostics (HMON) for multi-mode imaging and mild photo-therapeutic-induced mitochondrial damage on gastric cancer*. *J Nanobiotechnology*, 2020. **18**(1): p. 99.
45. Wang, L., et al., *Coordination-Accelerated "Iron Extraction" Enables Fast Biodegradation of Mesoporous Silica-Based Hollow Nanoparticles*. *Adv Healthc Mater*, 2017. **6**(22).
46. Fan, W., et al., *Generic synthesis of small-sized hollow mesoporous organosilica nanoparticles for oxygen-independent X-ray-activated synergistic therapy*. *Nature communications*, 2019. **10**(1): p. 1241.
47. Wang, L., et al., *Coordination-Accelerated "Iron Extraction" Enables Fast Biodegradation of Mesoporous Silica-Based Hollow Nanoparticles*. *Advanced healthcare materials*, 2017. **6**(22).
48. Jia, T., et al., *Intelligent Fe-Mn Layered Double Hydroxides Nanosheets Anchored with Upconversion Nanoparticles for Oxygen-Elevated Synergetic Therapy and Bioimaging*. *Small (Weinheim an der Bergstrasse, Germany)*, 2020. **16**(46): p. e2001343.
49. Zhou, J., et al., *Dual-Effect of Magnetic Resonance Imaging Reporter Gene in Diagnosis and Treatment of Hepatocellular Carcinoma*. *International journal of nanomedicine*, 2020. **15**: p. 7235-7249.
50. Chen, Q., et al., *Tumor Microenvironment-Responsive Nanococktails for Synergistic Enhancement of Cancer Treatment via Cascade Reactions*. *ACS applied materials & interfaces*, 2021. **13**(4): p. 4861-4873.
51. Tacar, O., P. Sriamornsak, and C. Dass, *Doxorubicin: an update on anticancer molecular action, toxicity and novel drug delivery systems*. *The Journal of pharmacy and pharmacology*, 2013. **65**(2): p. 157-70.
52. Yu, H., et al., *Ferroptosis, a new form of cell death, and its relationships with tumourous diseases*. *J Cell Mol Med*, 2017. **21**(4): p. 648-657.
53. Capelletti, M.M., et al., *Ferroptosis in Liver Diseases: An Overview*. *Int J Mol Sci*, 2020. **21**(14).

## Figures

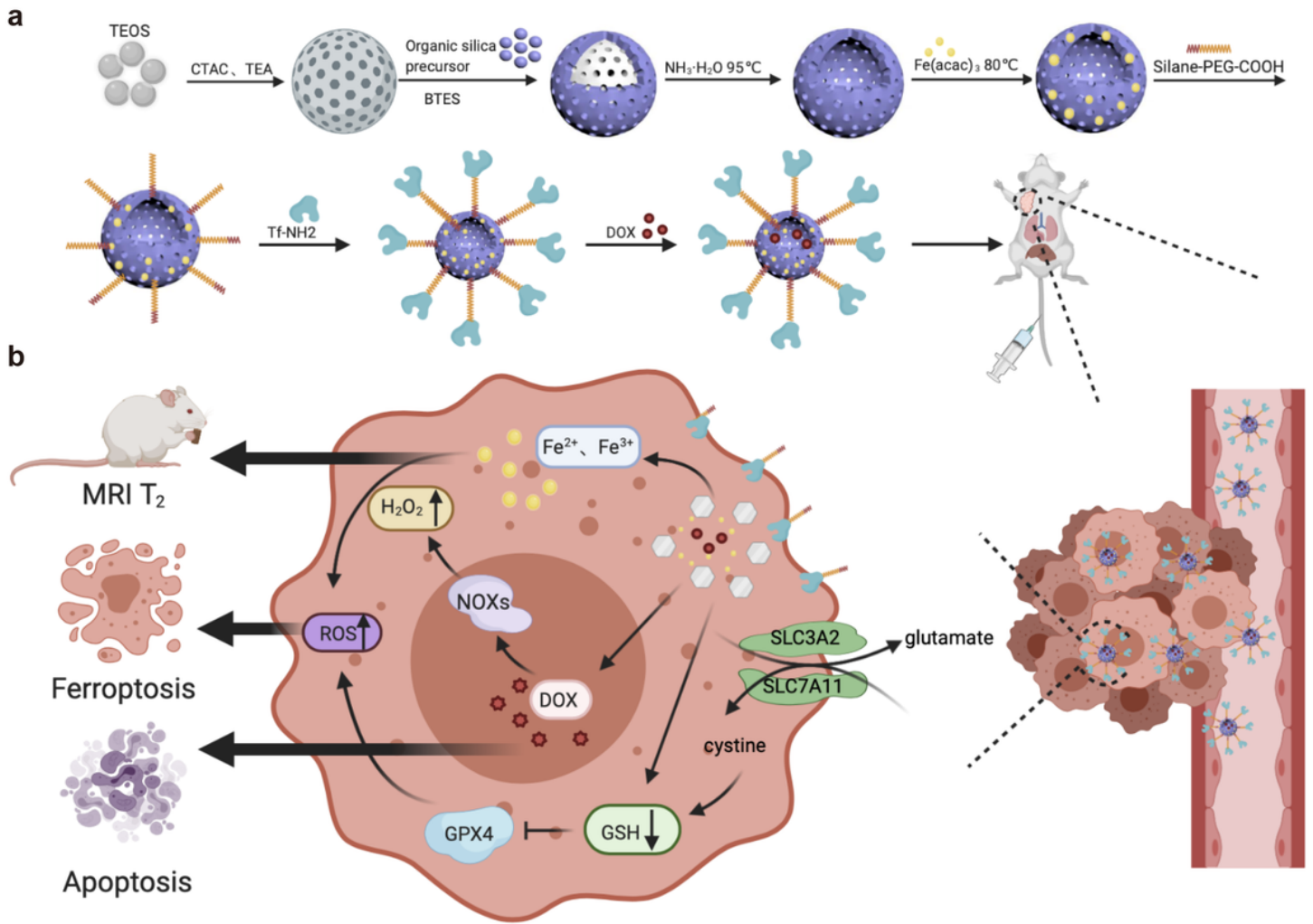


**Figure 1**

Synthesis and biomedical application of DOX@Fe-HMON-Tf NPs. a Schematic illustration of the preparation of DOX@Fe-HMON-Tf NPs. b Schematic diagram of the treatment and monitoring process of DOX@Fe-HMON-Tf NPs.

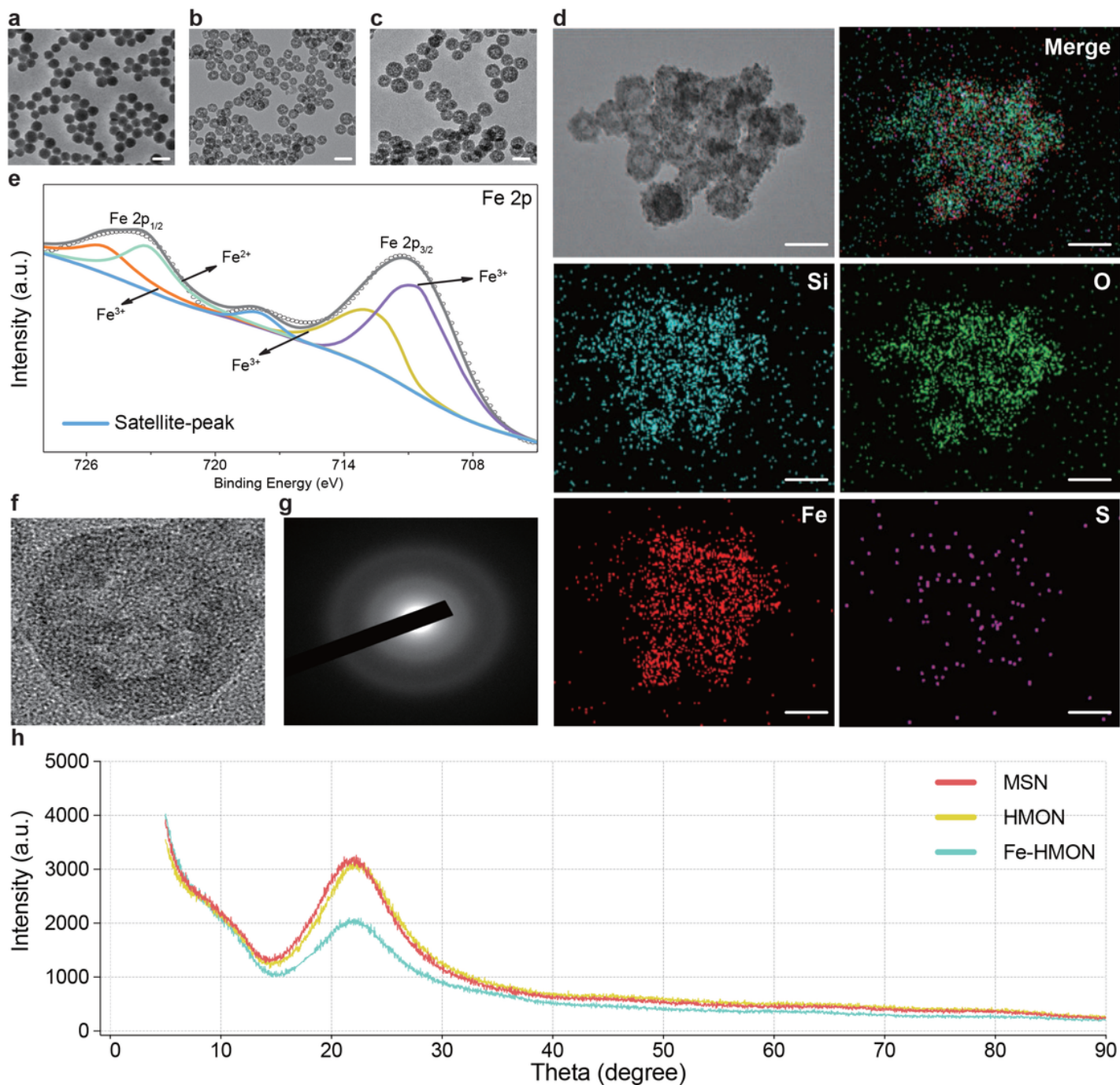


**Figure 2**

Structural and compositional characterizations of the nanoplateforms. a-c TEM images of the unetched HMON NPs, HMON NPs, and Fe-HMON NPs. Scale bar = 100nm. d High-resolution transmission electron microscopy images of Fe-HMON NPs and Elemental mapping (Si, O, Fe, S) in Fe-HMON NPs. Scale bar = 50nm. e Fe2p x-ray photoelectron spectroscopy (XPS) spectra of Fe-HMON NPs. f High-resolution transmission electron microscopy images of Fe-HMON NPs. g Selected area electron diffraction pattern of Fe-HMON NPs, indicating the amorphous nature of Fe-HMON NPs. h XRD patterns of MSN NPs, HMON NPs and Fe-HMON NPs.

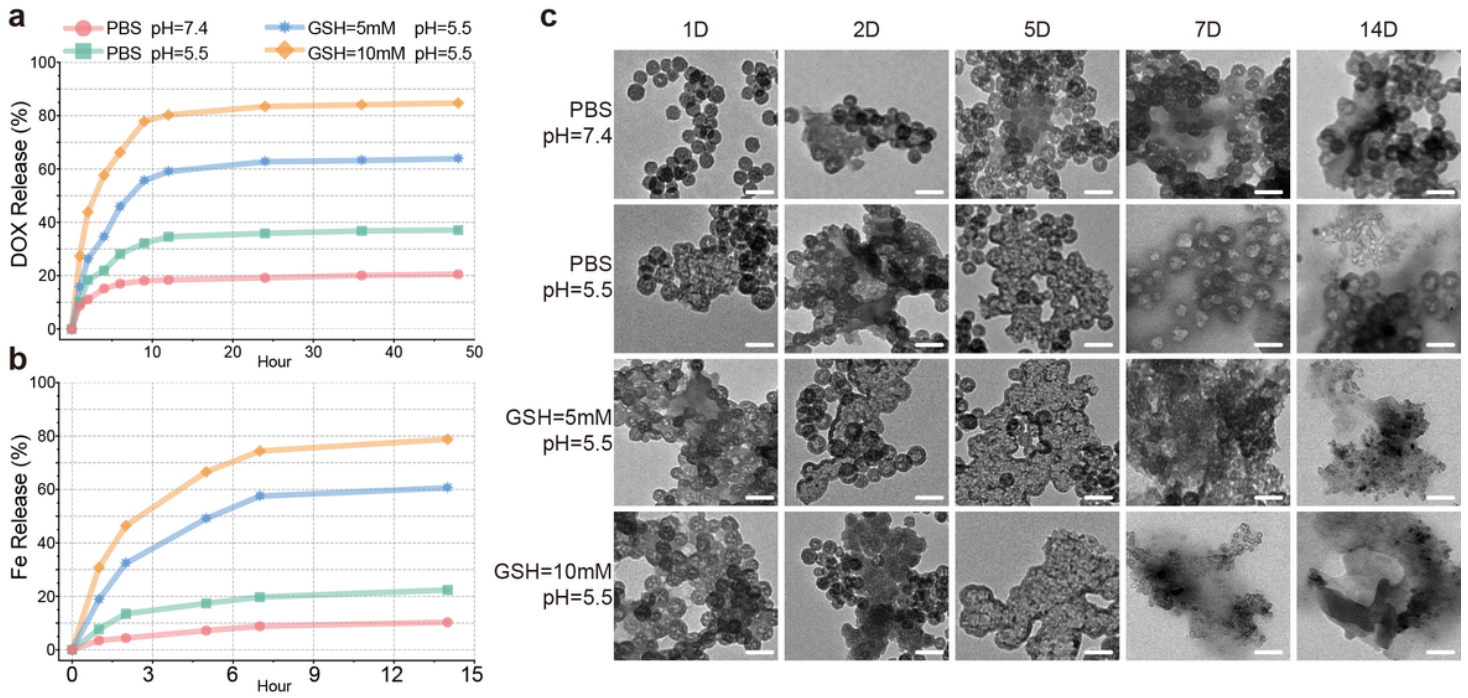


**Figure 3**

The simulated tumor microenvironment triggers the release characteristics of DOX and iron ions and the appearance of the nanoplatforms under the TEM. a The DOX release profiles from DOX@Fe-HMON-Tf NPs with or without different GSH concentrations under pH 7.4 and pH 5.5. b Accumulated degradation profiles of Fe species in PBS in varied pH and different concentrations of GSH conditions. c TEM images of Fe-HMON NPs in PBS with or without different GSH concentrations under neutral (pH=7.4) and acidic (pH=5.5) conditions at varied time intervals (1d, 3d, 5d, 7d and 14d). Scale bar = 100nm.

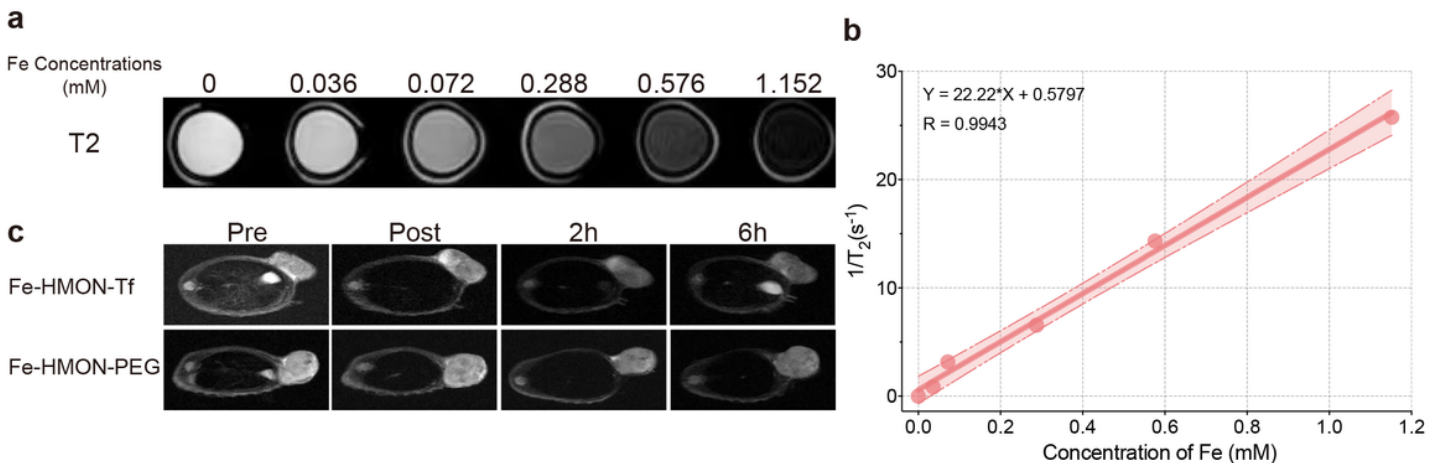


**Figure 4**

T2 MRI capabilities of the nanoplatforms. a T2-weighted solution MR images of DOX@Fe-HMON-Tf NPs of varied Fe concentrations (0, 0.036, 0.072, 0.072, 0.288, 0.576, 1.152mM). b T2 relaxation versus Fe concentration of DOX@Fe-HMON-Tf NPs in PBS solution. c In vivo T2-weighted MRI of HepG2 tumor-

bearing nude mice before and after the intravenous administration of DOX@Fe-HMON-Tf NPs for prolonged time intervals.

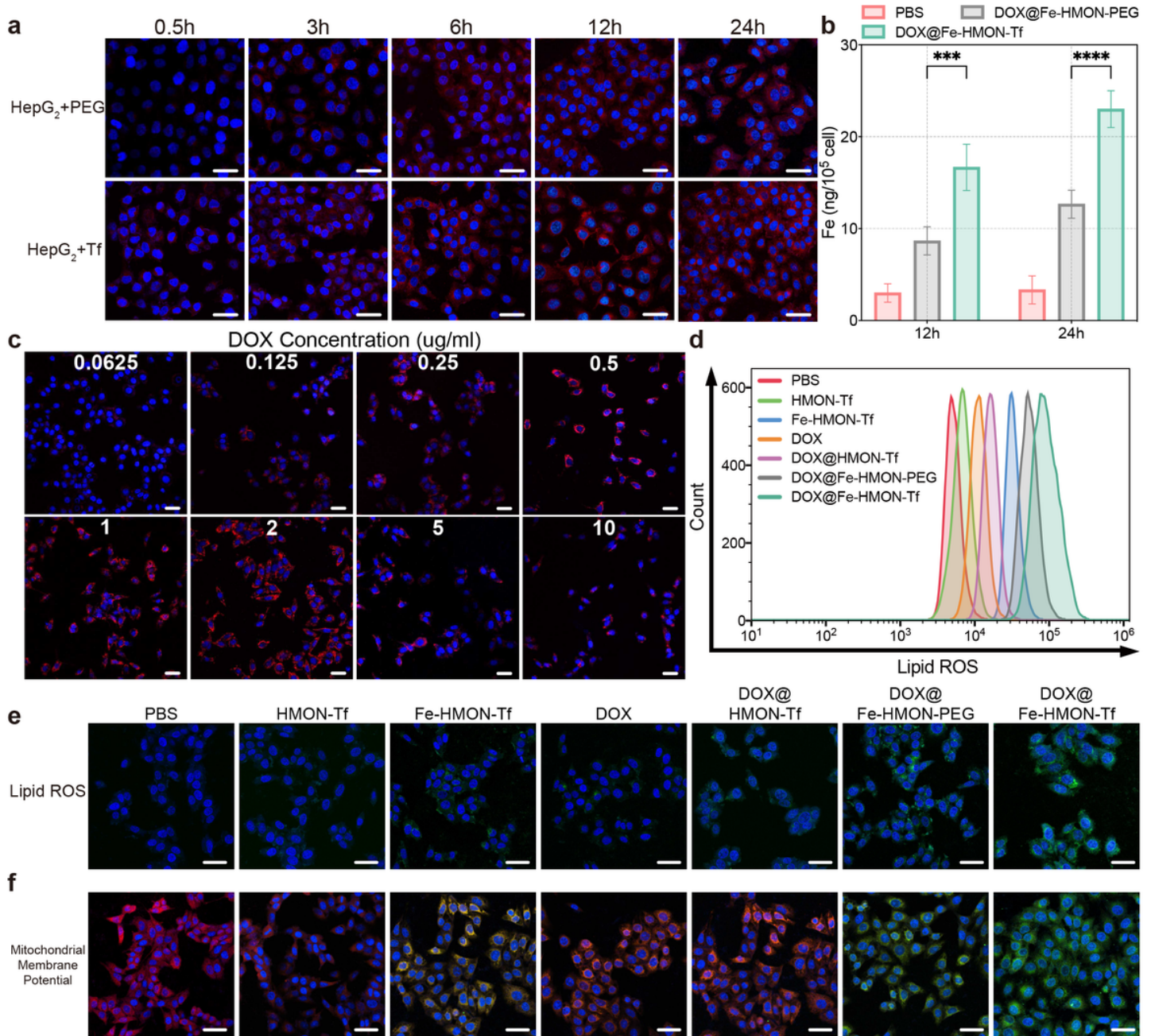


**Figure 5**

In vitro uptake and ROS generation capacity of nanoformulations. a CLSM images of HepG2 cells incubated with DOX@Fe-HMON-PEG NPs and DOX@Fe-HMON-Tf NPs for 24h. The blue and red colors indicate cell nucleus and the DOX-loaded nanoparticles, respectively. b ICP results on the intracellular iron levels of HepG2 cells after incubation with DOX@Fe-HMON-PEG NPs and DOX@Fe-HMON-Tf NPs for 24h. \*\*\*P < 0.001, \*\*\*\*P < 0.0001, Kruskal–Wallis test. c CLSM images of the intracellular H<sub>2</sub>O<sub>2</sub> levels of HepG2 cells incubated with varied concentrations of DOX for 24h. d-e Flow cytometric analysis and CLSM observation on the intracellular lipoperoxide levels in HepG2 cells incubated with PBS, DOX, HMON-Tf NPs, Fe-HMON-Tf NPs, DOX@HMON-Tf NPs, DOX@Fe-HMON-PEG NPs and DOX@Fe-HMON-Tf

NPs for 24h. The lipid ROS indicator was BODIPY-C11. f CLSM observation on the changes in the mitochondrial membrane potential of HepG2 cells after incubation with PBS, DOX, HMON-Tf NPs, Fe-HMON-Tf NPs, DOX@HMON-Tf NPs, DOX@Fe-HMON-PEG NPs and DOX@Fe-HMON-Tf NPs for 24h. Scale bar = 50um.

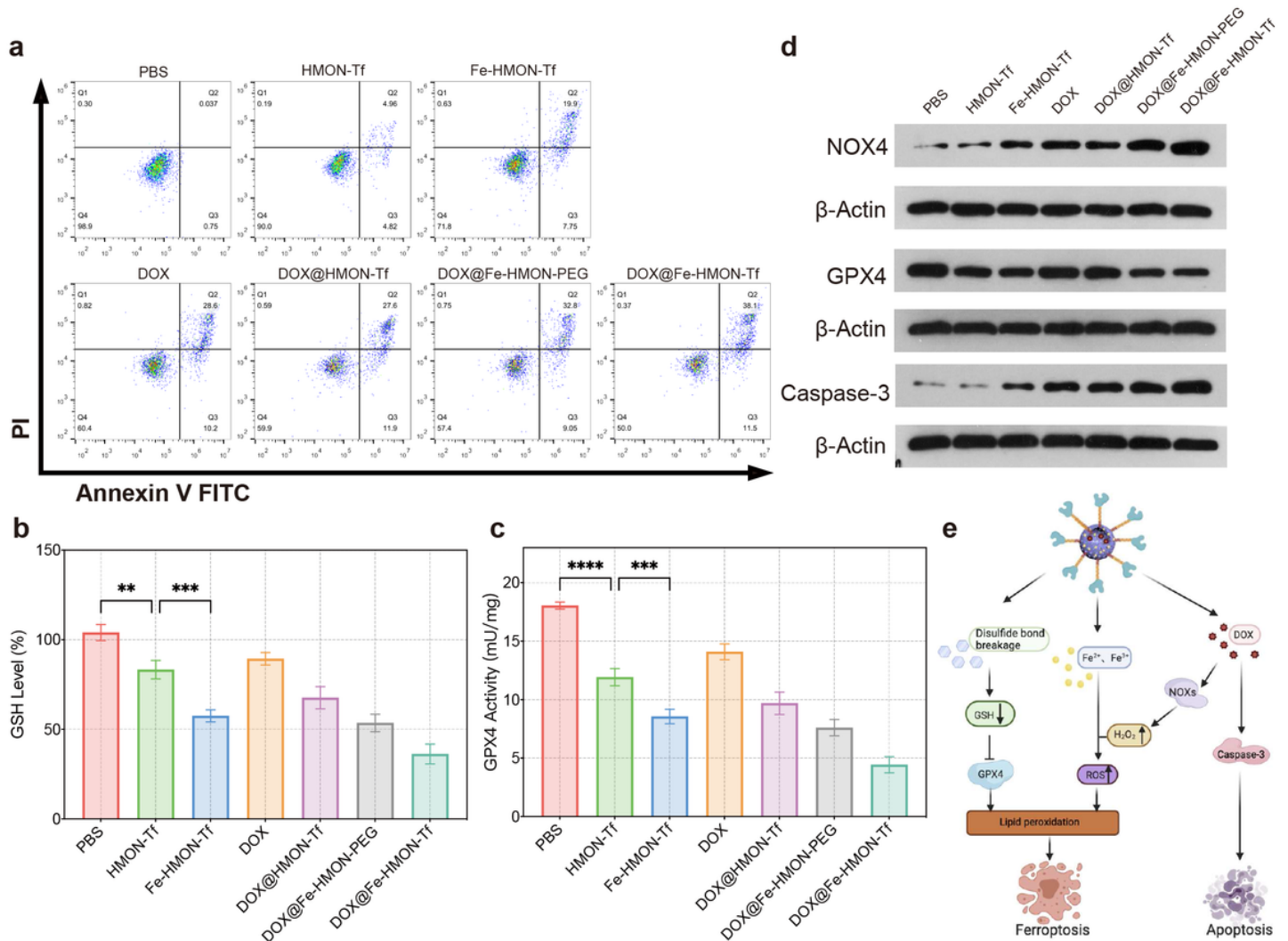


**Figure 6**

In vitro anti-tumor effect evaluation and mechanism exploration of nanoplateforms. a Flow cytometric analysis on the apoptosis levels of HepG2 cells after incubation with PBS, DOX, HMON-Tf NPs, Fe-HMON-Tf NPs, DOX@HMON-Tf NPs, DOX@Fe-HMON-PEG NPs and DOX@Fe-HMON-Tf NPs for 24 hours. b GSH levels in HepG2 cells after incubation with PBS, DOX, HMON-Tf NPs, Fe-HMON-Tf NPs, DOX@HMON-Tf NPs, DOX@Fe-HMON-PEG NPs and DOX@Fe-HMON-Tf NPs for 24h. \*\*P < 0.01, \*\*\*P < 0.001, Kruskal–Wallis test. c GPX4 activity in HepG2 cells after incubation with PBS, DOX, HMON-Tf NPs, Fe-HMON-Tf NPs, DOX@HMON-Tf NPs, DOX@Fe-HMON-PEG NPs and DOX@Fe-HMON-Tf NPs for 24h. \*\*\*P < 0.001, \*\*\*\*P < 0.0001, Kruskal–Wallis test. d Western blot analysis on the expression of key ferroptosis maker GPX4 as well as apoptosis markers including NOX4 and Caspase-3 in HepG2 cells after incubation with PBS, DOX, HMON-Tf NPs, Fe-HMON-Tf NPs, DOX@HMON-Tf NPs, DOX@Fe-HMON-PEG NPs and

DOX@Fe-HMON-Tf NPs. e The proposed molecular mechanism for the nanoplatform-induced synergistic ferroptosis and apoptosis.

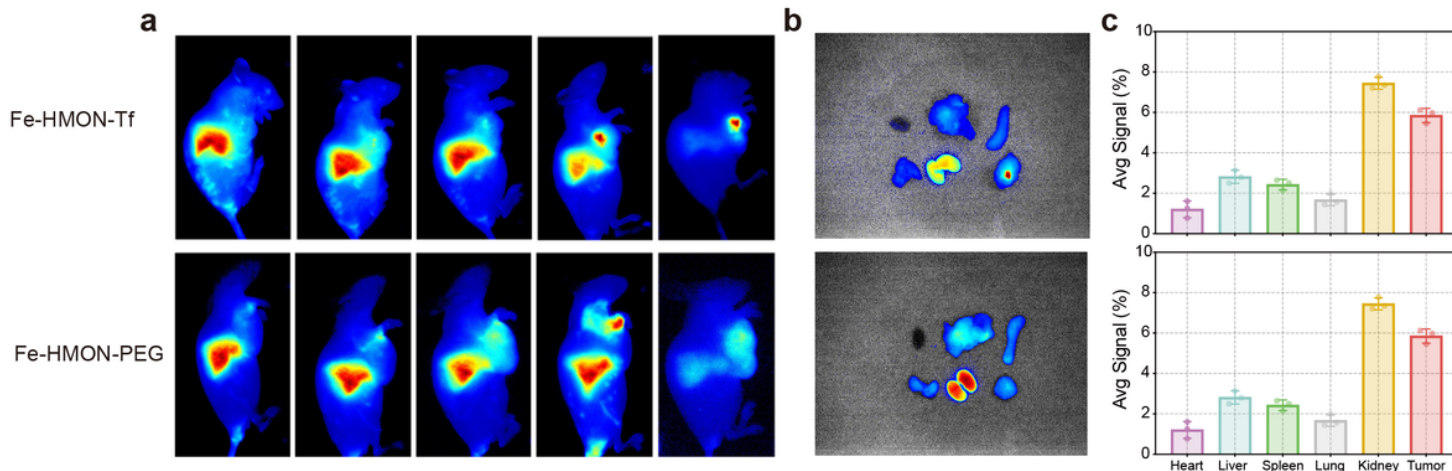


**Figure 7**

Fluorescence investigation on the distribution patterns of the nanoplatforms in tumor-bearing nude mice. a Fluorescence images of HepG2 tumor-bearing nude mice after the intravenous injection of DOX@Fe-HMON-PEG NPs and DOX@Fe-HMON-Tf NPs at different time points. b Ex vivo fluorescence images of organs and tumors harvested at 24h for mice bearing HepG2 tumors. c The fluorescence intensity of harvested tissue at 24h post-injection.

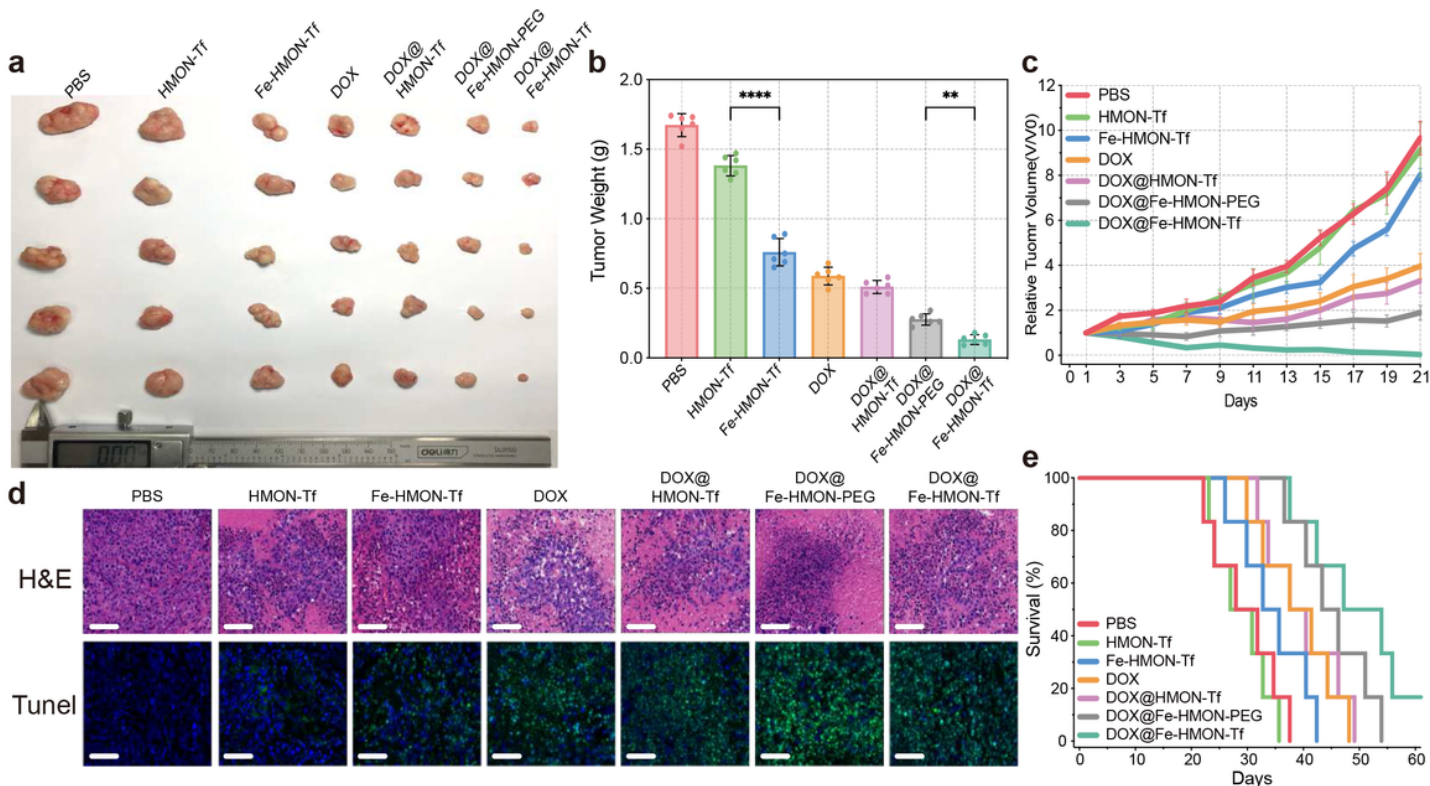


**Figure 8**

In vivo therapeutic efficacy of nanoplatfoms. a Comparison of tumor tissues extracted from HepG2 tumor-bearing mice after the 21 days treatment with PBS, DOX, HMON-Tf NPs, Fe-HMON-Tf NPs, DOX@HMON-Tf NPs, DOX@Fe-HMON-PEG NPs and DOX@Fe-HMON-Tf NPs. b Final weight of tumor tissues extracted from HepG2 tumor-bearing mice after the 21 days treatment with PBS, DOX, HMON-Tf NPs, Fe-HMON-Tf NPs, DOX@HMON-Tf NPs, DOX@Fe-HMON-PEG NPs and DOX@Fe-HMON-Tf NPs. \*\*P < 0.01, \*\*\*\*P < 0.0001, Kruskal–Wallis test. c Changes in the tumor volumes of the HepG2 tumor-bearing mice (six mice in each group) plotted against time, the tumor volume was measured every 2 days. d Histological analysis of the tumor slices under H&E and TUNEL staining after treatment with PBS, DOX, HMON-Tf NPs, Fe-HMON-Tf NPs, DOX@HMON-Tf NPs, DOX@Fe-HMON-PEG NPs and DOX@Fe-HMON-Tf NPs. Scale bar = 100um. e Survival rate of HepG2 tumor-bearing mice in 60 days (six mice in each group).

## Supplementary Files

This is a list of supplementary files associated with this preprint. Click to download.

- [SupplementaryFigure17.pdf](#)
- [GraphicalAbstract.pdf](#)